doi:10.20944/preprints202007.0433.v1

Cu-Doped KCl Unfolded Band Structure and Optical Properties Studied by DFT Calculations.

Cesar Castillo-Quevedo[1], Jose Luis Cabellos[2*], Raul Aceves[2,], Roberto Núñez-González[3] , and Alvaro Posada-Amarillas[2*]

[1]Departamento de Fundamentos del Conocimiento, Centro Universitario del Norte, Universidad de Guadalajara, Carretera Federal No. 23, Km. 191, C.P. 46200, Colotlán, Jalisco, México

[2]Departamento de Investigación en Física, Universidad de Sonora, Blvd. Luis Encinas y Rosales S/N, 83000 Hermosillo, Sonora, México.

[3]Departamento de Matemáticas, Universidad de Sonora, Blvd. Luis Encinas y Rosales S/N, 83000 Hermosillo, Sonora, México.

*Corresponding authors: jose.cabellos@unison.mx, posada@cifus.uson.mx

Abstract

The unfolded band structure and optical properties of Cu-doped KCl crystals were computed by first principles within the framework of density functional theory, implemented in the ABINIT electronic structure package utilizing pseudopotential approximation and a plane-wave basis set. From a theoretical point of view, Cu substitution into pristine KCl crystals requires calculation by the supercell (SC) method. This procedure shrinks the Brillouin zone, resulting in a folded band structure that is difficult to interpret. To solve this problem and gain insight into the effect of copper ions (Cu+) on electronic properties, the band structure of SC KCl:Cu was unfolded to make a direct comparison with the band structure of the primitive cell (PC) of pristine KCl. To understand the effect of Cu substitution on optical absorption, we calculated the imaginary part of the dielectric function of KCl:Cu through a sum-over-states formalism and broke it down into different band contributions by partially making an iterated cumulative sum (ICS) of selected valence and conduction bands. Consequently, we identified those interband transitions that give rise to the absorption peaks due to the Cu+ ion. These transitions involve valence and conduction bands formed by the Cu-3d and Cu-4s electronic states.

Keywords: DFT calculations, unfolding band structure, optical spectrum, KCl.

1. Introduction

Alkali halide (AH) crystals are solids of great importance from theoretical and experimental points of view. They are of great research interest in solid-state physics [1], mainly due to their high stability [2]. Pure AH crystals are relatively easy to produce in large quantities. They possess high melting points, varying from 600 to 1000 °C [3], are poor conductors of heat [2], and have strong miscibility in polar media [4]. They are also the most ionic of all crystal compounds [2] that consist of ions bound together by electrostatic attraction, making them good candidates for studying other systems [5]. The AH crystals have a large energy gap in the order of 8–10 eV, making them useful for the development of laser optical components as optical transmission windows in the ultraviolet (UV) to infrared (IR) ranges of the electromagnetic spectrum [3,6], among other optical applications. AH crystals, either pure or doped, are also employed as neutron monochromators [3].

Potassium chloride (KCl) is an inorganic salt with properties similar to those of common salt (NaCl). KCl is employed in optical windows for laser applications [8], and as a scintillator or in dosimetry by adding impurities [9–11]. At the end of the 1960s, several experimental and theoretical studies on the optical properties of KCl and other AH crystals were presented [12–19]. Recently, theoretical predictions on novel KCl phases under pressure have been proposed [20]. Several studies have addressed doping of KCl with monovalent cations, e.g., Ga^+, In^+, and Tl^+, to investigate distortion trends as a function of impurity [21]. Furthermore, recently published works show an enhancement in the optical properties of KCl crystals when doped with ZnO [11]. In other previous works, the optical properties of KCl crystals doped with Sb_2O_3 nanocrystals were investigated, analyzing the doping effects of the Sb_2O_3 nano-semiconductor on the optical properties of KCl crystals [22]. The optical properties of copper ion (CU+)-doped KCl and other AH crystals have also been studied due to their outstanding UV-light absorption properties [23–25], a characteristic that makes them excellent phosphor materials for many technological applications [26–28]. In the Cu+-doped KCl, several absorption bands in the UV region have been observed, with a strong dependence on temperature

doi:10.20944/preprints202007.0433.v1

[23,29]. These bands have been attributed to $3d^{10}\rightarrow3d^{9}4s^{1}$ transition states of Cu+. Theoretical calculations of the oscillator strength of Cu+ $3d^{10}\rightarrow3d^{9}4s^{1}$ transitions in NaCl hosts were performed to verify this conclusion [30]. Recently, Density Functional Theory (DFT) calculation of the electronic and optical properties of LiF:Cu+ was carried out, employing the CASTEP code within the pseudopotential approximation and reporting the formation of a band in the middle of the electronic bandgap due to copper (Cu) [31]. Despite the remarkable efforts that have been made to elucidate the electronic structure and origin of the absorption and emission spectra of the Cu+ ion embedded in KCl and other AH crystals, this has still not been achieved, and further theoretical studies with different models and methodologies are needed.

In this paper, we report the results of DFT calculations of the band structure, density of states, and optical properties of the Cu^{+} ion embedded in KCl. To study and identify the effects that impurities have on its electronic structure, we unfolded the band structure of KCl:Cu and compared it with that of pristine KCl. The band-to-band contribution to the optical spectrum is examined by partially summing selected bands using the sum-over-states formalism [32], which is employed in the evaluation of the imaginary part of the linear electric susceptibility tensor. The transitions between valence and conduction bands that are responsible for the effects of Cu substitution on the absorption of KCl are thus identified. The remainder of this paper is organized as follows: Section 2 briefly outlines the theory and provides the computational details. Section 3 presents a detailed discussion of the results of the unfolding and folding band structure, density of states, and band-to-band contribution to the optical response of pristine KCl and doped KCl:Cu system. Conclusions are given in Section 4.

2 Theoretical methods and computational details

KCl is an ionic crystal with a rock salt structure (NaCl). The face-centered cubic (FCC) crystalline structure phase of KCl belongs to the space group (Hermann–Mauguin) Fm3m (number 225) and point group (Hermann–Mauguin) m3m. In this structure, an octahedron of six counterions surrounds each ion; hence, the coordination number is six for both the anion, Cl^-, and cation, K^-. The experimental lattice constant is 6.29 Å [3,33–35]. Figure 1(a) shows the FCC primitive cell (PC) of pristine KCl, with two atoms at the base; the cation K^- is located at the [0,0,0] position, and the anion Cl^- is located at the [1/2,1/2,1/2] position, for which the Brillouin zone (BZ) is a truncated octahedron [36,37], and its primitive vectors are [0, 1/2,1/2], [1/2,0,1/2], and [1/2,1/2,0]. Figure 1(b) shows a larger FCC pristine system that contains eight times as many atoms as in the PC, so the number of atoms is 16 (8 Cl^- and 8 K^-). This cubic phase was obtained by accurately multiplying the PC lattice constants of KCl by 2 x 2 x 2. As a result, the lattice vector length became twice that of the original unit cell of the PC and had the same primitive vectors. This system allows us to make Cu substitutions, doping the KCl structure. Figure 1(c) shows an FCC doped system that contains eight anions of Cl^-, seven cations of K^+, and one monovalent cation of Cu^+, occupying the [0,0,0] position of the substituted cation K^+. The six Cl^- anions surrounding the monovalent Cu^+ cation are asymmetric.

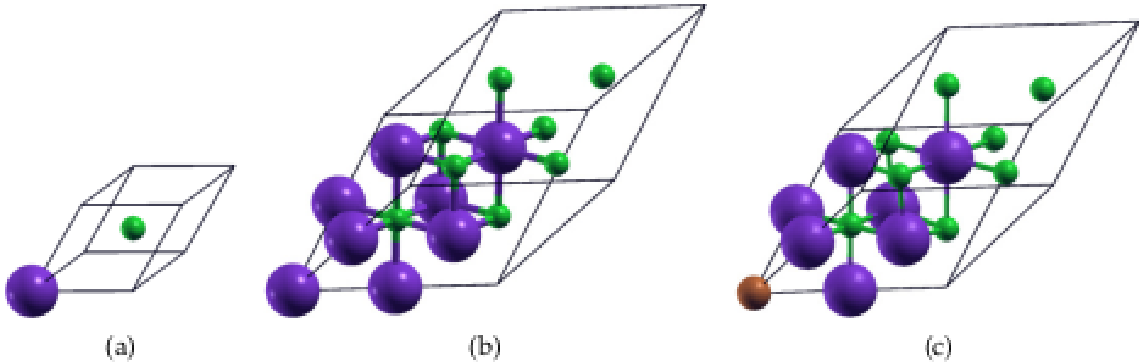

Figure 1. (a) Pristine face-centered cubic (FCC) primitive cell of KCl with two atoms at the base, (b) 2 × 2 × 2 pristine FCC supercell of the KCl with 16 atoms at the base, and (c) FCC supercell of KCl doped with Cu+ atom with 16 atoms at the base. The violet-, green-, and copper-colored spheres represent the potassium, chlorine, and copper atoms, respectively. The unit cell size and size of the atoms are depicted proportionally.

With this doped system, we can calculate the optical and electronic properties, and the electronic and optical properties of the pristine supercell (SC)/PC work as a reference system to observe the effect of the Cu^+ ion. Particular attention should be paid to the SC method of calculation. This method conveniently allows the folding of the bands into the smaller SC BZ that gives rise to a complicated band structure for which it is difficult to determine whether the bandgap is direct or indirect [38,39]. Moreover, other physical quantities, such as carrier mobility [40], require knowledge of the PC band structure. Several authors have already recently developed theories and methods with diverse approximations to unfold the SC band structure into a PC band structure, with successful results [39,41–53]. In this study, the unfolding of the SC BZ into the PC BZ was performed using the BandUP code [39,49,50], which is based on the evaluation of the spectral weight, $P_{mK}(k)=\sum_n \left|\psi_{nk}^{PC}\,\middle|\,\psi_{nK}^{SC}\right|^2$, where $|\psi_{nk}^{PC}\rangle$ and $\langle\psi_{mK}^{SC}|$ are the eigenstates of the PC and SC, respectively and $P_{mK}(k)$ is the spectral weight. This method gives the probability that an eigenstate of a Hamiltonian, in the SC representation, will have the same character as a PC state. This unfolding procedure of the SC BZ has been successfully employed in several systems, such as SiGe nanowires [38], graphene [54,55], and ternary alloys [56].

The optical absorption spectrum is determined by the dielectric function, $\varepsilon(\omega)$[57], which is related to the electric susceptibility $\left[\chi_1^{ab}(-\omega;\omega)\right]$ [58] by $\varepsilon(\omega)=1+4\pi\left[\chi_1^{ab}(-\omega;\omega)\right]$. The imaginary part of the electric susceptibility is given by:

$$\Im\left[\chi_1^{ab}(-\omega;\omega)\right]=\frac{e^2}{h}\int\frac{d^3k}{8\pi}\sum_{n\neq m} f_{nm} r_{nm}^{a}(k) r_{mn}^{b}(k)\delta(\omega_{mn}-\omega) \qquad [1]$$

In Eq. 1, e and h are the elementary charge and Planck's constant, respectively; n and m are the occupied initial and occupied final states $f_{mn}=f_m-f_n$; , with f_i as the Fermi occupation factor, which is zero or unity for cold semiconductors; $\omega_{mn}(\bar{k}) = \omega_m(\bar{k}) - \omega_n(\bar{k})$ are the frequency differences, where $\omega_m(\bar{k})$ is the DFT energy of band m at wave vector $\bar{k}$; and $r^a_{nm}(\bar{k})$ are the matrix position elements of bands m and n at vector $\bar{k}$. Following the procedure of a previous work [32], in this study, we computed the expression given in Eq. 1. The peaks, presented in the $\Im[\chi_1^{ab}(-\omega;\omega)]$ part, are due to the direct interband optical transitions between the valence and conduction bands, which can be identified from the critical points of the band structure. Moreover, in this study, the bands that can contribute significantly to the $\Im[\chi_1^{ab}(-\omega;\omega)]$ part are identified by breaking down the $\Im[\chi_1^{ab}(-\omega;\omega)]$part into different band contributions [59,60]. In addition, we considered the scissor correction [32,61], the approximation of which is obtained by a rigid shift of the DFT energies to an experimental value [62]. Therefore, the spectrum of $\Im[\chi_1^{ab}(-\omega;\omega)]$ is rigidly shifted along the energy axis without changing the spectrum shape [32,61]. The real part $\Re[\chi_1^{ab}(-\omega;\omega)]$ was computed using Kramers–Kronig relations [63]. Here, the indirect transitions are neglected because they have little contribution [64] to $\Im[\chi_1^{ab}(-\omega;\omega)]$, and the spin–orbit, local field, and electron–hole effects are also neglected [32,65]. The inclusion of these effects is beyond the scope of this study.

The electronic and optical properties are calculated using the SC approach in the DFT framework, as is implemented in the freely available ABINIT code [66,67]. We chose the optimized norm-conserving Vanderbilt (ONCV) pseudopotentials [68] taken from the *ONCVPSP-PBE-PD v0.4* library, following Ref. [66]. These were validated against all-electron calculations and found to perform well. Among these pseudopotentials, the $3s^2 3p^6 3d^{10} 4s^1$, $3s^2 3p^6 4s^1$, and $3s^2 3p^5$ electrons of the Cu, K, and Cl atoms, respectively, are treated as valence states. We employed the Perdew–Burke–Ernzerhof (PBE) general gradient approximation functional to calculate the exchange-correlation energy [69].

Table 1. Parameters employed in the present study’s calculation.

Unit cell	**Number of *k*-points**	**Size grid**	**Energy cutoff (Ha)**
(a) KCl	3864	55×55×55	25
(b) K_8Cl_8	2920	19×19×19	25
(c) K_7Cl_8 :Cu	2920	19×19×19	25

The wavefunctions were expanded in a plane-wave basis set and checked for convergence by applying a kinetic cutoff energy of 25 Ha. The Monkhorst–Pack scheme [70] was used to sample the irreducible Brillouin zone (IBZ). The IBZ integration was performed by employing the tetrahedron method [32]. Table 1 shows the number of the chosen *k*-points, cutoff energy, and *k*-point mesh corresponding to the system, to assure convergence of the total energy and forces as well as the optical properties. The total energy of the self-consistent field (SCF) procedure was set to a value of 5×10^{-7} eV/atom. All the atomic positions of the studied systems were relaxed until the Hellmann–Feynman forces on each atom were lower than 20 meV/Å. The resulting atomic structures were used for all the calculations presented in this study.

3. Results and discussion

3.1. Optimized lattice constant

We computed the PC KCl lattice constant through minimization of the total energy by employing the parameters shown in Table 1. The obtained result was 4.507 Å for the FCC PC system, which is in agreement with the experimental lattice constant of 6.29 Å [3,33–35]— larger by 1.22% — and is slightly shorter—by 0.3%—compared with other theoretical calculations that obtained 4.522 Å [71]. It is more similar to other calculations that used an all-electron scheme [28] (see Table 2).

Table 2 Lattice constant and bandgap obtained in the DFT calculation.

Unit cell		Lattice constant (Å)	Bandgap (eV)
(a)	KCl	4.507	5.07
(b)	K_8Cl_8	9.014	5.07
(c)	K_7Cl_8:Cu	8.390	2.20

The FCC supercell of the pristine system K_8Cl_8 is eight times the volume of the primitive cell of KCl. In Table 2, the lattice constant of the SC two times greater than the lattice constant of the PC. After the optimization of the K_7Cl_8:Cu system, the resulting unit cell is FCC with its three optimized lattice parameters measuring 8.390 Å, and its three lattice angles being 60°. The optimized volume of the pristine K_8Cl_8 is 472.0 Å^3, and the volume of K_7Cl_8:Cu is 417.7 Å^3. The SC volume of the doped system is 11.5% smaller, which is evidently due to copper doping (in Figure 1, this can be seen in the proportions of the unit cells). For this system, the calculated density of Cu based on its atomic weight and the volume of the unit cell with an 8.390 Å edge length is 0.25 g/cm^3. The unit cell has five non-equivalent atoms, and the distances between the Cu atom and the ions surrounding it are shorter by approximately 0.43 Å. The optimized bond length of K–Cu is 2.651 Å compared to the bond length of K–Cl atoms (3.090 Å) in the pristine system.

3.2 Electronic band structure and density of states

The band structure of the pristine KCl has been reported previously [28,35,71]. For comparison, in later sections with the doped system, we show in Figure 2(a) the band structure of the PC for KCl computed along high-symmetry directions in the BZ, from the BZ center Γ with the coordinates (0,0,0) to the X point (0,0.5,0.5), W point (0.25,0.5,0.75), K point (0.375,0.375,0.75), Γ point

(0.0,0.0,0.0), L point (0.0,0.0,0.5), U point (0.0,0.375,0.625), W point (0.25,0.5,0.75), L point (0.0, 0.0,0.5), U point (0.0,0.375,0.625), and X point (0.0 0.5 0.5) in units of $2\pi/a, 2\pi/b, 2\pi/c$, where *a*, *b*, and *c* are the lattice constants shown in Table 2. Figure 2 (b) shows the unfolded band structure of the pristine SC K_8Cl_8. The lowest direct Kohn–Sham band gap of the KCl obtained in both calculations is ~5.07 eV, at the Γ point, as indicated by the red arrow in Figure 2(a) and 2(b) (displayed in Table 2) and in agreement with previous calculations [35,71].

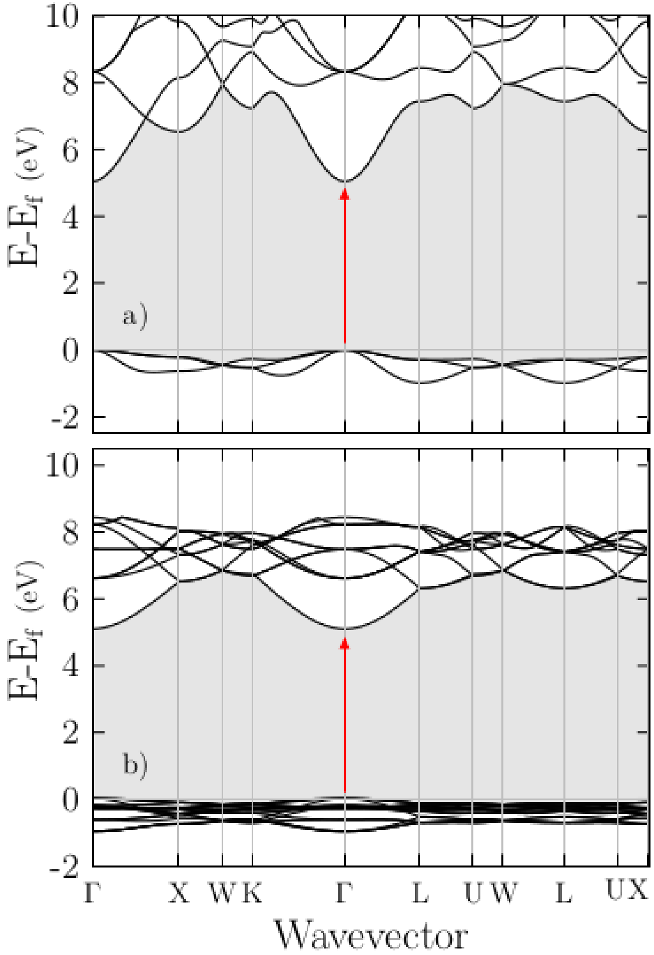

Figure 2. The upper panel (a) shows the band structure of the primitive cell (PC) for KCl. The lower panel (b) shows the folded band structure of the supercell (SC) of K_8Cl_8 along with the same high-symmetry directions of the Brillouin zone (BZ) of the PC. The shortest direct Kohn–Sham bandgap indicated by the red arrow is ~5.07 eV at the Γ point in both plots.

In these calculations, the bandgap is underestimated by ~3.53 eV compared with the experimental value of 8.6 eV [72,73] of the KCl, and other recently reported all-electron DFT calculations using the modified Becke–Johnson approximation [28]. To correct the bandgap that was underestimated by DFT [74], we applied a scissor correction of 3.53 eV to the conduction bands, which shifted them to the experimental value. Following and comparing the results presented in Figure 2(a) and 2(b), it can be seen that the principal difference is the band dispersion in the K–Γ–L direction, although we consider the same crystal. This difference is due to SC shrink of the BZ; thus, one should not wrongly conclude something that depends on the dispersion of the band structure (e.g., the effective mass) using an SC band structure.

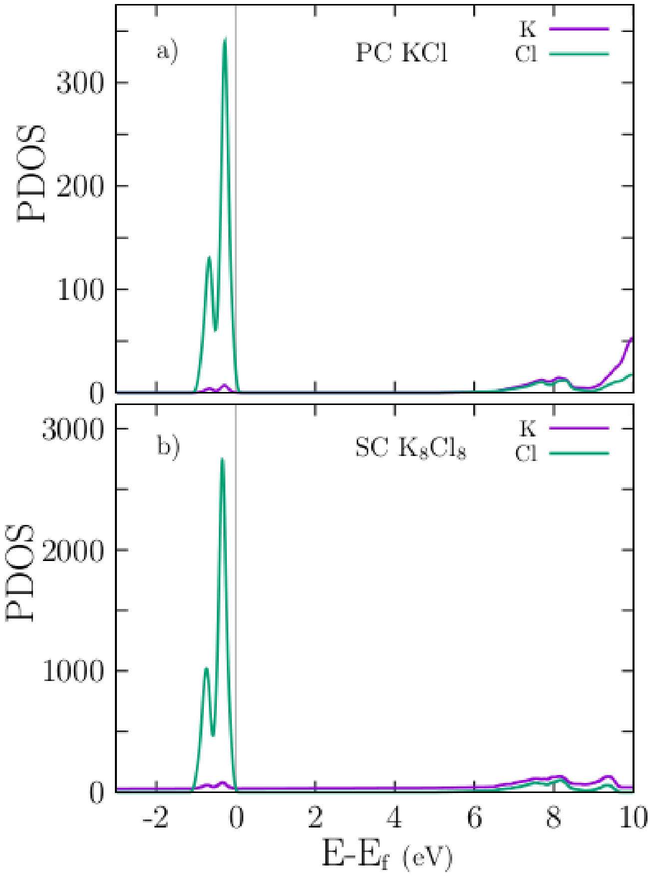

Figure 3. The upper panel (a) shows the projected density of states (PDOS) for the pristine PC for KCl. The

lower panel (b) shows the PDOS for the pristine SC of K_8Cl_8. In both plots, the Cl-3p states dominate at the Fermi level. Notice the main difference: the density is higher in the SC than in the PC system. The color code is violet for K and green for Cl.

To elucidate the nature of the electronic band structure, we calculated the projected density of states (PDOS) as a function of energy for the pristine PC KCl (Figure 3 (a)), SC K_8Cl_8 (Figure 3 (b)), and doped SC K_7Cl_8:Cu (Figure 5(a), (b), and (c)) structures. In those plots, the Fermi energy is shifted to zero. For the pristine PC and SC, our results are in good agreement with those of previous studies [28]; notice that the density of PDOS for the SC is higher than that for the PC. The examination of the PDOS shows that the width of valence bands is approximately 1 eV, which is in agreement with the folded band structure shown in Figure 2(b). The highest valence bands are mainly formed by the Cl-3p states, which are in line with previous studies [35]. Just slightly below the Fermi level, there are tiny contributions of K-3p states, as can be seen from the PDOS plot in Figure 3. Thus, there is a slight admixture (not an overlap) between the Cl-3p states and a few K-3p states, as expected for an ionic compound. Meanwhile, at approximately 5 eV, the bottom conduction bands have contributions from both the K-4s and Cl-4s states.

3.3. Folded band structure of the doped K_7Cl_8:Cu

The effect of the Cu atom on the electronic properties was analyzed. Figure 4(a) shows the folded band structure for the doped K_7Cl_8:Cu system, along the same high-symmetry path used in the calculation for the pristine PC KCl. Figure 4(b) shows a zoomed view of the folded band structure in the range of −4.0 to 0.5 eV, where the dispersionless character of the bands located at the (shifted) Fermi level can be clearly observed. The lowest calculated direct Khon–Sham bandgap is 2.2 eV at the Γ point.

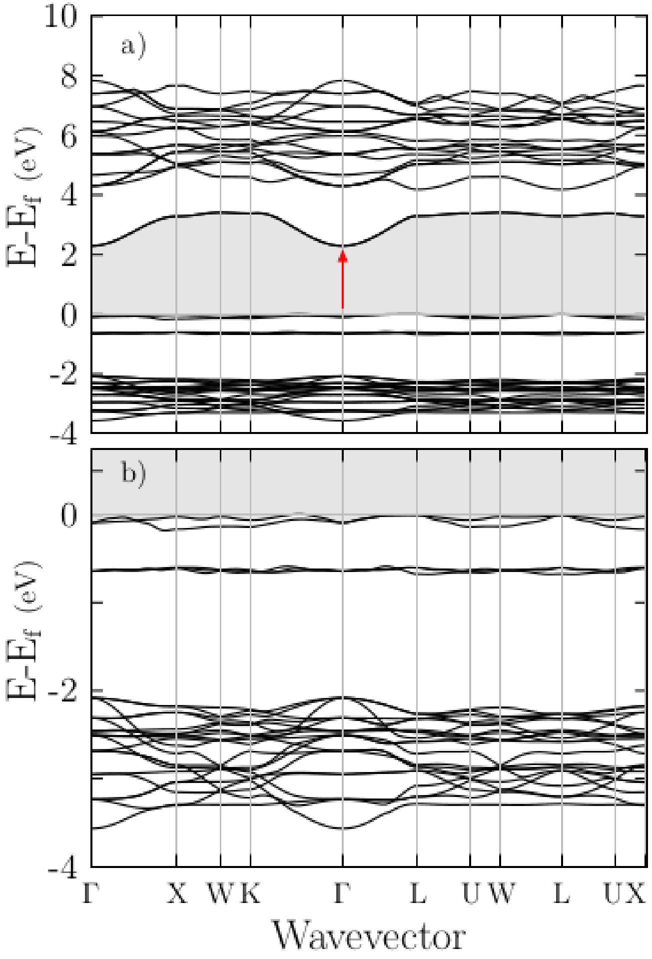

Figure 4. The upper panel (a) shows the calculated folded band structure of SC K_7Cl_8:Cu along the same high-symmetry directions of the BZ used in the PC. The lower panel (b) shows a zoomed region in the energy range of 4.0 to 0.5 eV. The lowest direct Kohn–Sham bandgap, indicated by the red arrow, is about 2.2 eV at the Γ point.

Partial DOS is plotted in Figure 5(a-c) for Cl, K, and Cu atoms, respectively. Cl and K atoms present small p-state contributions at the Fermi level, as shown by Figure 5(a) and (b). A closer examination of the PDOS for the Cu ion plotted in Figure 5(c) reveals two sharp peaks located around the Fermi level, the maxima of which are shifted by ~0.6 eV compared to one another. The two topmost valence bands are formed by Cu-3d states and a couple of sub-bands, shown in Figure 4(b), clearly localized at 0.6 eV below the Fermi level. They are also composed of Cu-3d states, as the PDOS indicates. In the energy range of −2.0 to −4.0 eV, there are many bands bunched together with a dispersionless character, as is clearly shown in Figure 4. These bands are also mainly composed of Cl-3p states, as the PDOS reveals. In the energy range of 2 to 4 eV, there are also many bands bunched together with a dispersionless character. These bands are mainly composed of K-d states, as the PDOS reveals. The bottom conduction band also has a dispersionless character and is composed solely of Cu-s states.

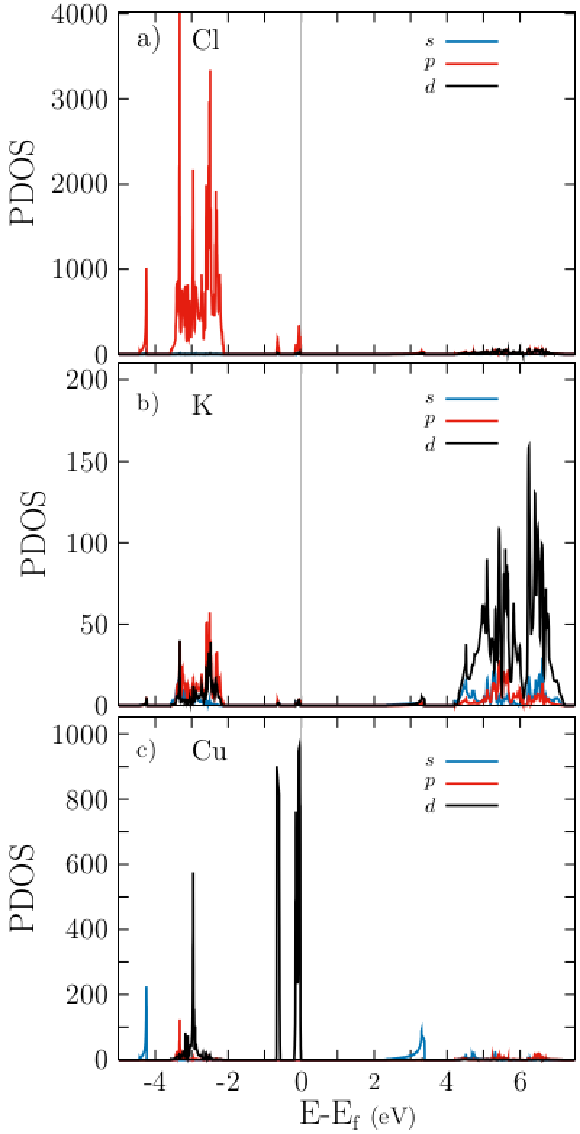

Figure 5. The upper panel (a): PDOS for the Cl atom. Middle panel (b): PDOS for the K atom. The lower panel (c): PDOS for the Cu atom. The Cu-3d states dominate at the Fermi level with a sharply peaked density, and at 2.2 eV, the Cu-4s states dominate. For all atoms, s-, p-, and d-states are identified by light blue, black, and red

lines, respectively.

3.3 Unfolded band structure of pristine K_8Cl_8 and doped K_8Cl_8:Cu

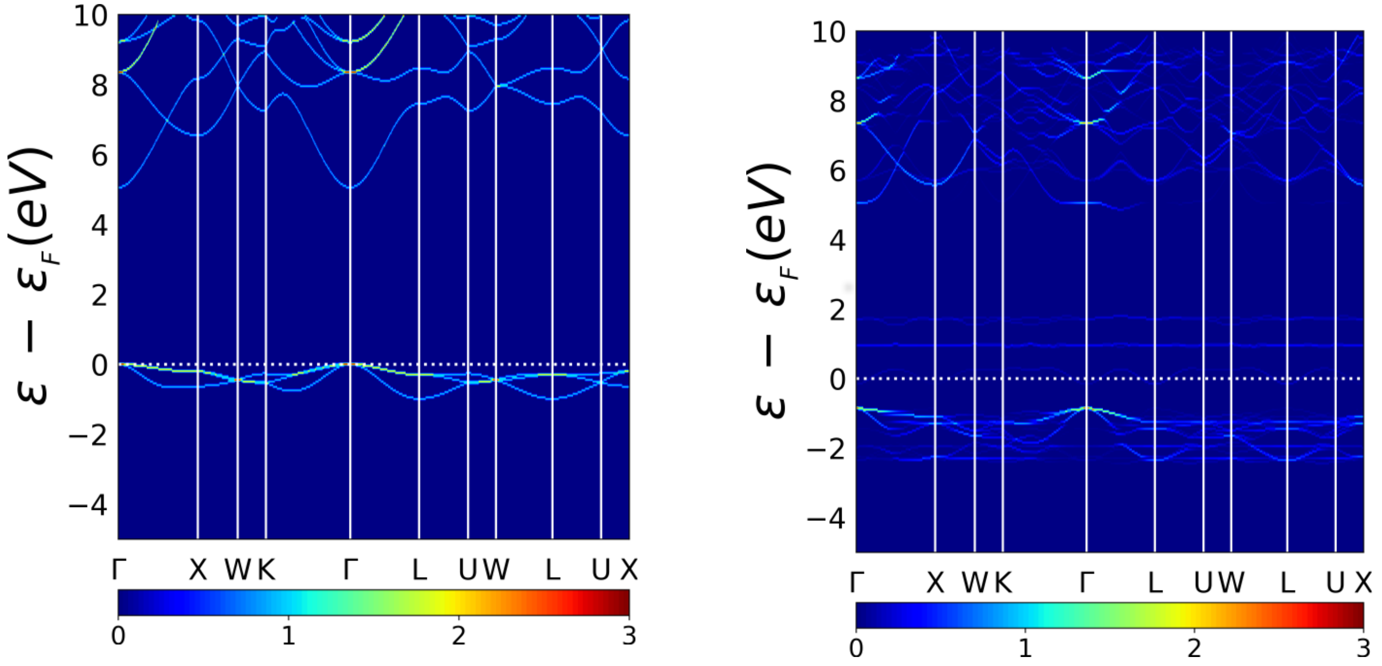

Figure 6. Effective band structure (EBS) for pristine SC K_8Cl_8 (left panel) and EBS for doped SC K_7Cl_8:Cu (right panel), along with the same high-symmetry directions in the BZ and the same energy range. The color scale represents the number of PC bands crossing the energy interval (0.05 eV) at a given primitive wave vector [41,51,78].

To gain a better understanding of the Cu atom doping effects on the KCl at the electronic level, we unfolded the band structure of the doped SC K_8Cl_8:Cu. To perform a test and make a comparison with the doped system, we also unfolded the pristine SC K_8Cl_8. The left panel of Figure 6 shows the unfolded band structure for pristine SC K_8Cl_8 or the so-called effective band structure (EBS), introduced by Popescu [39,43] and other researchers [49,75,76]. The EBS can be directly compared to Angle-Resolved Photoemission Spectroscopy (ARPES) data [55]. The EBS for the pristine SC K_8Cl_8 should give the exact eigenvalues obtained from the band structure calculation employing PC KCl. We found the band structures of the PC and SC KCl to be identical due to the perfect translation of the primitive cells that built the pristine SC K_8Cl_8. To facilitate mutual comparison, the EBS shown in Figure 6 was computed within the same energy range and high-symmetry directions in the BZ employed in the band structure of PC KCl, as shown in Figure 2(a). The EBS of the doped SC K_8Cl_8:Cu is depicted in the right panel of Figure 6. As shown in this figure, the effect of Cu doping on the electronic structure of pure KCl is dramatic. As shown in the right panel, the Cu doping greatly modifies the electronic structure of KCl, narrowing the energy bandgap and opening small gaps in the valence and conduction bands. The Fermi level has shifted to zero energy axes.

A detailed examination of Figure 6 indicates that Cu-doping of the KCl structure reduces the direct energy bandgap and that the unfolding procedure preserves the same direct character of the energy bandgap (Figure 4). Previous studies suggest that the folded bands fail to reproduce the indirect bandgap character [38,77]. The cutoff of the energy bandgap is attributed to the appearance of empty bands with a dispersionless character located at 1.0 and 2.0 eV. The right panel of Figure 6 shows the existence of a single valence band located at the Fermi level with small peaks and valleys; despite these, the band is quite flat, thus producing a pronounced peak in the PDOS. Further analysis of the valence bands reveals bunched-together bands in the energy range of −3.0 to −1.0 eV, showing many small energy gap openings that are not observed in the folded band structure of the SC K_8Cl_8:Cu, shown in Figure 2(b). Interestingly, similar energy gap openings were found in bi-graphene studies [55]. Moreover, a small gap appeared in the bottom conduction bands at an energy of 5.0 eV, located at the Γ–L valley. A direct comparison between the bottom conduction band of pristine EBS (left panel of Figure 6) and the bottom conduction band of the doped EBS (right panel of Figure 6) shows that significant changes occurred in the k–Γ–L valley, which drastically changed the band dispersion and opened small gaps, as mentioned before.

3.4 Optical properties

Optical properties (OP) are a valuable source of atomic structural information, and their electronic band structure largely determines them [79,80]. Once we obtained the optimized crystal structure of the KCl, the OPs were calculated by evaluating Eq. 1. Figure 7(a) shows the *xx* component of the imaginary $\Im\left[\chi_1^{xx}(-\omega;\omega)\right]$ part of the electric susceptibility tensor for the pristine PC KCl in the energy range of 0 to 20 eV, which is in good agreement with previous calculations [28].

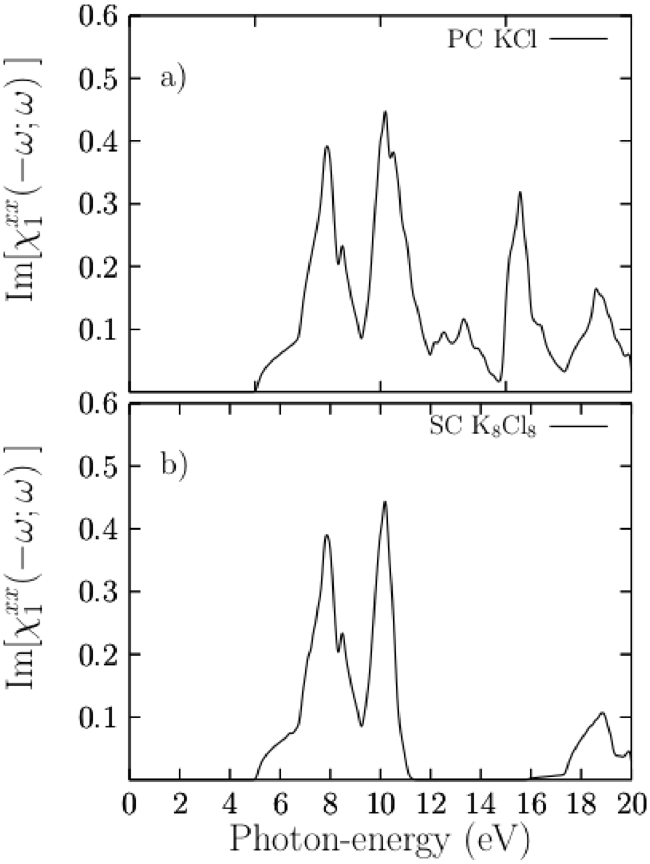

Figure 7. The upper panel (a) shows the calculated $\Im\left[\chi_1^{xx}(-\omega;\omega)\right]$ part corresponding to pristine PC KCl, with the FCC structure and two atoms in the base. The lower panel (b) shows the calculated $\Im\left[\chi_1^{xx}(-\omega;\omega)\right]$ corresponding to pristine SC K_8Cl_8, ($2\times2\times2$ pristine PC KCl), with 16 atoms in the base.

Figure 7 (b) shows the $\Im\left[\chi_1^{xx}(-\omega;\omega)\right]$ part for the pristine SC K_8Cl_8. As shown in this figure, the $\Im\left[\chi_1^{xx}(-\omega;\omega)\right]$ part starts to rise at 5.0 eV, and it has peaks located at 7.8, 10.2, 15.5, and 18.6 eV. There are minor peaks located at 8.4 and 13.3 eV. At the onset of the signal, there is a shoulder in the energy range of 5.0 to 6.7 eV, which is mainly due to the direct transitions from the topmost valence bands(highest-energy valence bands) at the Γ point. As the crystal structure of KCl is completely isotropic, the *xx*, *yy*, and *zz* components are also isotropic. Hereafter, we only present the *xx* component, and the scissor correction of 3.53 eV was applied at the end. The main difference between the PC and SC responses is located above 12.0 eV on the energy axis because the number of electronic bands necessary to converge the SC system is higher than that of the PC. Nonetheless, the signals are similar in the energy range of 5 to 10 eV. Figure S1 (a) and (b) (Supplementary Information) shows the real part of the pristine PC KCl and SC K_8Cl_8 systems. The real part provides information about the polarizability of the material. Figure S1 (a) shows that the static value $\Re\left[\chi_1^{xx}(-\omega;\omega)\right]$ is 0.1 $\left(\chi_1^{xx}(0)=0.1\right)$ for pristine PC KCl. From here, it starts to increase and reach a large peak with a value of 0.3 at 6.9 eV. After that, a rapid decrease is observed until it reaches zero. The negative values of the real part are observed in the energy range of 10.28 to 14.43 eV and above 15.5 eV. At 10.28 eV, the real part changes sign. The negative values of the real part are indicative of metallic behavior, whereas a change of sign in the real part indicates the occurrence of plasmonic resonances in the energy region where it crosses the energy axes with a positive slope. The real part for the pristine SC has a similar behavior.

3.5 Breakdown of the $\Im\left[\chi_1^{xx}(-\omega;\omega)\right]$ part of pristine SC KCl into different band contributions

Figure 8(a) shows the breakdown of the $\Im\left[\chi_1^{xx}(-\omega;\omega)\right]$ part, taking into account the transitions within an iterated cumulative sum (ICS) of all the valence bands, assigning to the top valence band the index 1 (VB_1), the sub-top valence band 2 (VB_2), and so on (e.g., $VB_{[1]}$, $VB_{[1+2]}$) against the single bottom conduction band (CB_1). In this in-house developed scheme, the first ICS corresponds to the contributions to the $\Im\left[\chi_1^{xx}(-\omega;\omega)\right]$ part due to the top valence and bottom conduction bands. The red line in Figure 8(a) clearly shows that the contribution to the onset of the signal up to 6.5 eV is 50%. The second ISC, which takes into account the top valence and sub-top valence bands against the single bottom conduction band, is depicted by the solid blue line in Figure 8(a), which clearly shows that this ICS contributes to the $\Im\left[\chi_1^{xx}(-\omega;\omega)\right]$ part by almost 95% for the onset of the signal. The rest of the ICS contributes only about 5%. Twenty of the ICSs are plotted and shown in Figure 8(a). Our calculated band contribution breakdown indicates that we only need the two topmost valence bands and the bottom conduction band to build up the onset of the signal of up to 6.5 eV with an accuracy of 95%. Moreover, based on the PDOS, the Cl-3p states mainly form the two topmost valence bands, and the bottom conduction band is composed of a mixture of Cl-s and K-s states. Therefore, the onset of the signal up to 6.5 eV is due to the direct transitions involving Cl-3p, Cl-4s, and K-4s states at the Γ point.

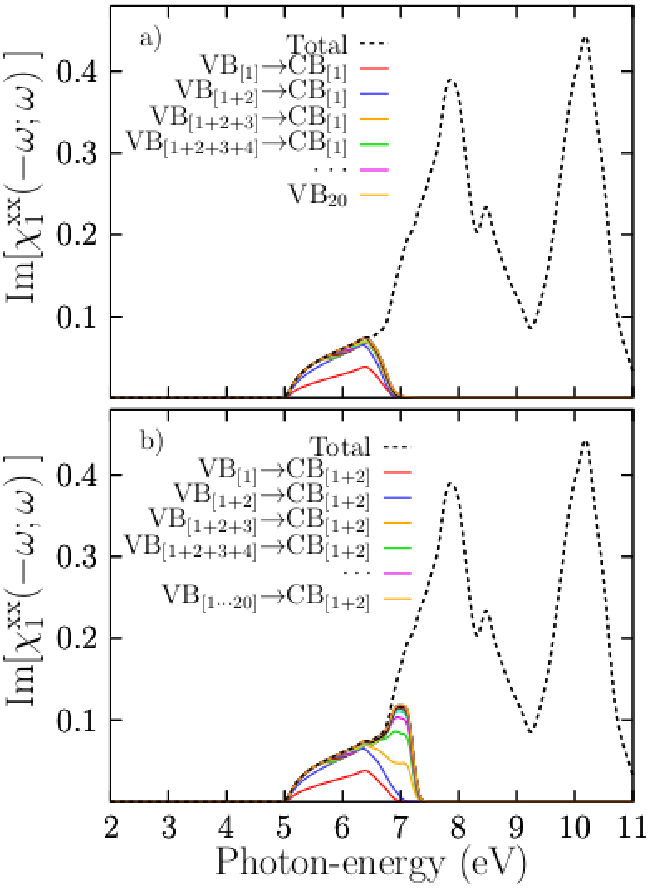

Figure 8. Breakdown of the imaginary part of the SC K_8Cl_8 into different band contributions. The upper panel (a) shows the decomposition of the $\Im\left[\chi_1^{xx}(-\omega;\omega)\right]$part by only considering the 20 highest

valence band (VB) transitions to only the first conduction band (CB), e.g., $VB_{[1]} \rightarrow CB_{[1]}$, $VB_{[1]+[2]} \rightarrow CB_{[1]}$, $VB_{[1]+[2]+[3]} \rightarrow CB_{[1]}$. The lower panel (b) shows the decomposition of the $\Im\left[\chi_1^{xx}(-\omega;\omega)\right]$ part only considering the 20 highest VB transitions to only the first and second CBs, e.g., $VB_{[1]} \rightarrow CB_{[1]+[2]}$, $VB_{[1]+[2]+[3]} \rightarrow CB_{[1]+[2]}$. The black dotted line in both panels represents the $\Im\left[\chi_1^{xx}(-\omega;\omega)\right]$ part, taking into account all VBs and CBs considered in the calculation.

Figure 8 (b) shows the breakdown of the $\Im\left[\chi_1^{xx}(-\omega;\omega)\right]$ part with an ICS considering all valence bands against the two bottom-most conduction bands. The figure shows that the contribution of the first ICS, depicted by the solid blue line, considers the transitions from the top valence band to the two bottom-most conduction bands, which are similar to those when we consider a single bottom conduction band. The third ICS, depicted as a solid yellow line in Figure 8(b), builds the large peak located at 7.8 eV. In summary, and to solve the first large peak located at 7.8 eV and peaks located at higher energies, we need to take higher conduction bands into account.

3.6 The $\Im\left[\chi_1^{xx}(-\omega;\omega)\right]$ part of the doped K_7Cl_8:Cu

Figure 9 shows the $\Im\left[\chi_1^{xx}(-\omega;\omega)\right]$ part that corresponds to the doped SC K_7Cl_8:Cu system depicted by the solid blue line, while the solid black line corresponds to the $\Im\left[\chi_1^{xx}(-\omega;\omega)\right]$ part of the pristine SC K_8Cl_8 system. We have included both signals on the same graphic to compare them. Figure 9 shows that doping KCl with Cu had a drastic effect on in its optical properties. The main peak starts to rise at 0.9 eV and ends at 4.0 eV and is composed of four sub-peaks located at 1.1, 1.87, 2.3, and 2.9 eV. In the energy range of 4.0 to 6.7 eV, there is a large peak located at 5.7 eV with little ripples. Above the energy range of 6.7 eV, the signals and peaks for the doped and pristine systems are similar, and those peaks are located at an energy of 7.8 eV. The larger peak observed in the pristine signal around 10 eV, and not observed in the doped system, is caused by the number of conduction bands considered in the calculation. Figure 1S (c) shows the $\Re[\chi_1^{xx}(-\omega;\omega)]$ part for the doped SC K_7Cl_8:Cu. It also clearly shows that the static value of the $\Re[\chi_1^{xx}(-\omega;\omega)]$ part is 0.22, $(\chi_1^{xx}(0)= 0.22)$, which is slightly more than double for the pristine case of 0.1. As a consequence, the refraction index of the doped SC K_7Cl_8:Cu, which is related to the static value of the dielectric function, can increase at around 70% compared with the pristine case.

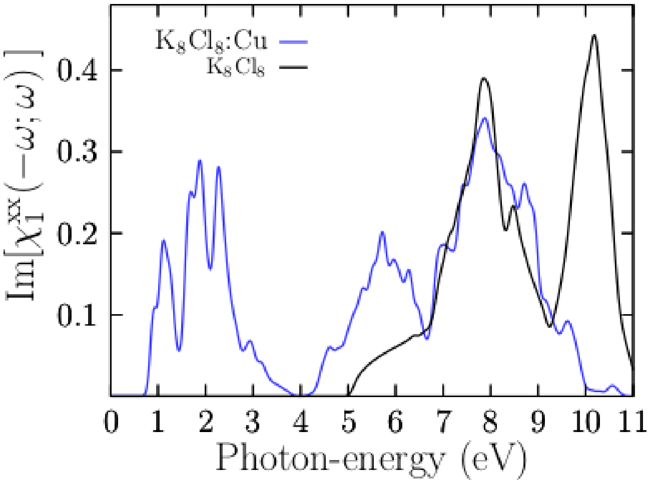

Figure 9. The solid blue line represents the $\Im[\chi_1^{xx}(-\omega;\omega)]$ part of the SC K_7Cl_8:Cu in the energy range of 0 to 11 eV. The black solid line represents the $\Im[\chi_1^{xx}(-\omega;\omega)]$ part of the pristine SC K_8Cl_8 system.

Figure 1S (c) also shows that the largest peak, with a value of 0.3, is located at 0.8 eV, followed by a rapid decrease until 0.15 at 1.31 eV, after starting to rise to form a large peak located at 1.6 eV. From here, it begins to decrease until it crosses zero at 2.3 eV. At this energy value, the real part changes sign, indicating an occurrence of plasmonic resonances. Negative values of the $\Re[\chi_1^{xx}(-\omega;\omega)]$ part are observed in the energy range of 2.30 to 2.70, 7.90 to 15.9 eV, and above 17.8 eV. Comparing the $\Re[\chi_1^{xx}(-\omega;\omega)]$ part of the pristine and the $\Re[\chi_1^{xx}(-\omega;\omega)]$ part of the doped case, we find significant differences, similar to those found in the imaginary parts.

3.7. Breakdown of the $\Im\left[\chi_1^{xx}(-\omega;\omega)\right]$ part of the doped SC K_7Cl_8:Cu into band contributions

To elucidate the transitions contributing to the peaks that are located in the energy range of interest, we depict, in Figure 10, the computed breakdown of the $\Im\left[\chi_1^{xx}(-\omega;\omega)\right]$ part into band contributions (see also the video in the supplementary material).

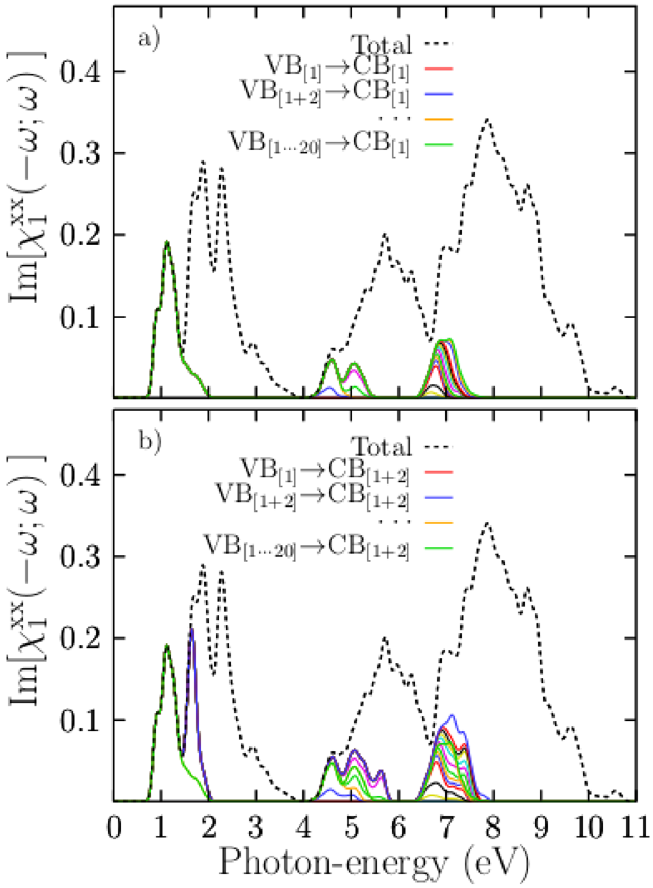

Figure 10. Breakdown of the $\Im\left[\chi_1^{xx}(-\omega;\omega)\right]$ part of the K_7Cl_8:Cu into different band contributions. The upper panel (a) shows the $\Im\left[\chi_1^{xx}(-\omega;\omega)\right]$ part, taking into account all valence bands with a single bottom conduction band. The lower panel (b) shows the $\Im\left[\chi_1^{xx}(-\omega;\omega)\right]$ part, taking into account all valence bands with the two bottom-most conduction bands. The black dotted line represents the total $\Im\left[\chi_1^{xx}(-\omega;\omega)\right]$ part, considering all valence and conduction bands available.

In Figure 10(a), the first ICS that involves the single top valence band ($VB_{[1]}$) and single bottom conduction band ($CB_{[1]}$) accounts for the entire peak of the $\Im\left[\chi_1^{xx}(-\omega;\omega)\right]$ part located at 1.1 eV.

Following the calculated PDOS presented in Figure 5(c), the top valence band is dispersionless and is composed of Cu-3d states, while the bottom conduction band is mainly composed of Cu-s states. Thus, the first peak of the $\Im\left[\chi_1^{xx}(-\omega;\omega)\right]$, located at 1.1 eV, is caused by the transitions of Cu-3d to Cu-4s, mainly at the Γ point. For Cu-s states at around 2.2 eV, this figure also shows a PDOS with a low density of states, implying a broader bottom conduction band. In contrast, the same PDOS shows a very high density of states located at the Fermi level, indicating a relatively narrow valence band. Our calculations show that the intraband transitions take place from a dispersionless band composed of Cu-3d states to the bottom conduction band formed by Cu-4s states. Our calculated Kohn–Sham bandgap for the pristine case is 5.07 eV, which is an underestimation of 59% compared with the experimental value of 8.6 eV. If we consider this 59% to estimate the correct bandgap of the doped system, we obtain 3.90 eV; therefore, the first peak of the $\Im\left[\chi_1^{xx}(-\omega;\omega)\right]$ should be located at 3.17 eV, in excellent agreement with previous works [23]. Experimentally, it has been corroborated that there is a transition for copper, located at 2.2 eV, which explains why the copper has a reddish color. [81] Considering our calculations and the shift to 3.17 eV of the first absorption peak, the doped system should have a violet color due to the transitions between the top valence band, formed by Cu-3d states, and the bottom conduction band, formed by Cu-4s states. The second ICS that involves the topmost and second-topmost valence bands ($\mathrm{VB}_{[1+2]}$) and the single bottom conduction band ($\mathrm{CB}_{[1]}$) is depicted in the solid blue line of Figure 10(b). This transition contributes to the first peak located at 1.1 eV and the peak at 4.3 eV. Therefore, the peak located at 5.7 eV is also due to the Cu-3d states. The ICS involving valence bands with 3 to 5 indices account for the small peaks located at 5.7 eV, and those that involve valence bands with 7 to 40 indices against the single bottom conduction band contribute to the most significant peak, located at 7.8 eV. According to the calculated PDOS shown in Figure 5(c), these valence bands are located in the energy range of −2.0 to −4.0 eV and are mainly composed of Cl-3p states. This peak begins with transitions from Cl-3p states to the bottom conduction band, which is composed of a mixture of Cu-4s.

To gain more insight into the optical absorption details, we now break down the $\Im\left[\chi_1^{xx}(-\omega;\omega)\right]$part considering the two bottom-most conduction bands against all the valence bands. The first ICS transition, taking into account the single top valence and two bottom conduction bands, is depicted as a solid red line in Figure 10(b). It provides the sole contribution to the first peak of the part located at 1.1 eV and contributes in part to a peak located at 1.87 eV. The behavior is similar to the case when we take a single bottom conduction band. Indeed, the four peaks of the $\Im\left[\chi_1^{xx}(-\omega;\omega)\right]$ part located at 1.1, 1.87, 2.3, and 2.9 eV involve transitions from the two topmost valence bands to the bottom conduction bands. The PDOS indicates that those transitions involve Cu-3d and K-3d states. In summary, the first peak located at 1.1 eV is initiated by the transitions between the top valence bands, formed by pure Cu-3d states, to the bottom conduction band, formed by Cu-4s states. The second peak, located at 1.87 eV, is associated with transitions from the topmost valence bands to the second bottom bands. Therefore, it is contributed to by transitions from the top valence band formed by pure Cu-3d states to the second conduction band formed by K-3d states (see Figure 4). The onset of the peak located at 5.7 eV is initiated by the transitions between bands formed mainly of Cl-3p states to conduction bands formed of Cu-4s. Indeed, transitions to conduction bands formed by K-3d states (located at 4 eV) must also occur to form this peak.

6. Conclusions

In summary, we employed the band structure unfolding technique to study the electronic properties and breakdown the imaginary part of the dielectric susceptibility of the pristine KCl and doped KCl:Cu systems to gain fundamental insights into the effect of copper doping on the electronic structure and optical properties of pure KCl. To study the changes in the band structure, we performed a direct comparison with the band structure of the pure KCl. In addition, we unfolded the band structure of the pure SC KCl, recovering the exact band structure of the PC KCl. Our findings show significant differences between the unfolded band structure of the Cu-doped KCl and the unfolded band structure of pure KCl. For the doped system, the bandgap was drastically reduced. Moreover, a dispersionless electronic band associated to Cu-3d states appears at the Fermi level, and the conduction bands above the Fermi level are attributed to the Cu-4s electronic states. There is also less dispersion in the bottom conduction band of the doped system and a large dispersion in the bottom conduction band for pristine KCl. In general, the main differences between the folded and the unfolded band structures of the doped KCl are the drastic change in the overall dispersion and the opening of small energy gaps in the bands, which were revealed by the unfolding procedure. The unfolding method was proven useful in the study of doped materials or those containing vacancies. To study the optical properties, we broke down the $\Im\left[\chi_1^{xx}(-\omega;\omega)\right]$ part into band contributions. The sum-over-states formalism allows one to decompose band-to-band contribution through partial band-index summation, the bands of which significantly contribute to $\Im\left[\chi_1^{xx}(-\omega;\omega)\right]$. This methodology, proposed here together with PDOS, allows us to identify and analyze the origin of the peaks presented in the $\Im\left[\chi_1^{xx}(-\omega;\omega)\right]$ part. Our findings for the doped case show that the first peak of $\Im\left[\chi_1^{xx}(-\omega;\omega)\right]$ located at 1.1 eV is due to transitions between the top valence band, which consists solely of Cu-3d states, to the bottom conduction band, formed of Cu-4s states. Therefore, the first peak is attributed to the transitions from Cu-3d to Cu-4s states. The second peak, located at 1.87 eV, is due to transitions between the top valence band and bottom conduction band. In addition, transitions between the top valence band and the sub-bottom conduction band were ascribed to K-3d states, i.e., the second peak of $\Im\left[\chi_1^{xx}(-\omega;\omega)\right]$ located at 1.87 eV is due to an admixture of electronic transitions from Cu-3d to Cu-4s states and from Cu-3d to K-3d states. We explain the origin of the onset of the signals and demonstrate that the methodology of decomposing the imaginary part into band contributions is a powerful tool in achieving a better understanding of the transitions participating in the optical response peaks.

AUTHOR CONTRIBUTIONS:

C.C.Q. performed the calculation and drafted the manuscript; J.L.C. performed calculations and analysis, drafted the manuscript; R.A. contributed to the conception of the study and drafted the manuscript; R.N.G. performed calculations and drafted the manuscript; A.P.A. contributed to the conception of the study, performed the data analyses, and revised the manuscript.

DECLARATION OF COMPETING INTEREST: The authors declare no conflict of interest.

FUNDING: This research was funded by Consejo Nacional de Ciencia y Tecnología (CONACYT), Mexico (grant number A1-S-39326).

ACKNOWLEDGMENT: Computational resources supporting this work were provided by ACARUS through the High-Performance Computing Area of the University of Sonora.

REFERENCES

[1] Bhandari, K.P. **Optical properties of alkali halides in ultraviolet spectral regions.** Optics 2019, 1, 18–31. doi:10.3390/opt1010002.

[2] Baldochi, S.; Ranieri, I. **Alkali halide crystals growth. In reference module in materials science and materials** Engineering; Elsevier, 2016. doi:https://doi.org/10.1016/B978-0-12-803581-8.02424-3.

[3] Sirdeshmukh, D.B.; Sirdeshmukh, L.; Subhadra, K.G. Alkali Halides: A **handbook of physical properties;** Springer, Berlin, Heidelberg, 2001. doi:https://doi.org/10.1007/978-3-662-04341-7

[4] Gopikrishnan, C.R.; Jose, D.; Datta, A. **Electronic structure, lattice energies and born exponents for alkali halides from first principles.** AIP Advances 2012, 2, 012131, [https://doi.org/10.1063/1.3684608]. Doi:10.1063/1.3684608.

[5] Zhang, C.; Andersson, T.; Svensson, S.; Bjorneholm, O.; Huttula, M.; Mikkela, M.H.; Tchaplyguine, M.; Ohrwall, G. **Ionic bonding in free nanoscale NaCl clusters as seen by photoelectron spectroscopy**. The Journal of Chemical Physics 2011, 134, 124507, [https://doi.org/10.1063/1.3570576] doi:10.1063/1.3570576.

[6] Chen, Z.; Xiao, H.; Zu, X. **First Principles Study of Structural, Electronic and Optical Properties of KCl Crystal.** Chemical Physics 2006, 330, 1–8. doi:https://doi.org/10.1016/j.chemphys.2006.04.017.

[7] Cepanec, K.; Vugrinec, S.; Cvetkovic, T.; Ranilovic, J. Potassium Chloride-Based Salt Substitutes: A Critical Review with a Focus on the Patent Literature. **Comprehensive Reviews in Food Science and Food Safety** 2017, 16, 881–894, [https://onlinelibrary.wiley.com/doi/pdf/10.1111/1541-4337.12291] doi:10.1111/1541-4337.12291.

[8] Palik, E. Handbook of Optical Constants of Solids, Five-Volume Set: **Handbook of Thermo-Optic Coefficients of Optical Materials with Applications**; Elsevier Science, 1997.

[9] Feridoun, S.; Ebrahim, H.A.; Somayeh, S.; P. Taravati, A. **KCl single crystals growth with Mn, Ag and In impurities by Czochralski method and study of impurities influence on their properties.** Open Journal of Physical Chemistry 2012, 2, 185–188, [10.4236/ojpc.2012.23025]. doi:10.4236/ojpc.2012.23025.

[10] Polosan, S.; Tsuboi, T.; Apostol, E.; Topa, V. **Electrolytic reduction of Tl+ ions in KCl crystals**. Optical Materials 2007, 30, 95 – 97. Selected papers from the 4th International Symposium on Laser, Scintillator and Nonlinear Optical Materials

[11] Shiehpour, M.; Solgi, S.; Jafar Tafreshi, M. **ZnO-doped KCl single crystal with enhanced UV emission lines.** Appl. Phys. A 2019, 125, 1–9, [https://doi.org/10.1007/s00339-019-2846-8]. doi:https://doi.org/10.1007/s00339-019-2846-8.

[12] Tomiki, T. Optical Constants and Exciton States in KCl Single Crystals. II**. The Spectra of Reflectivity and Absorption Constant.** Journal of the Physical Society of Japan 1967, 23, 1280–1296, [https://doi.org/10.1143/JPSJ.23.1280]. doi:10.1143/JPSJ.23.1280.

[13] Baldini, G.; Bosacchi, B. **Optical properties of alkali-halide crystals.** Phys. Rev. 1968, 166, 863–870. doi:10.1103/PhysRev.166.863.

[14] Baldini, G.; Bosacchi, A.; Bosacchi, B. **Exciton-phonon interaction in alkali halides.** Phys. Rev. Lett. 1969, 23, 846–848. doi:10.1103/PhysRevLett.23.846.

[15] Said, K.I.; Green, G.W. **Optical properties of caesium iodide in the vacuum ultraviolet**. Journal of Physics C: Solid State Physics 1977, 10, 479–488. doi:10.1088/0022-3719/10/3/018.

[16] Philipp, H.R.; Ehrenreich, H. **Intrinsic optical properties of alkali halides**. Phys. Rev. 1963, 131, 2016–2022. doi:10.1103/PhysRev.131.2016.

[17] Blechschmidt, D.; Klucker, R.; Skibowski, M. **Dielectric properties of KCl, KBr, and KI single crystals in the extreme ultraviolet up to 35 eV.** Pphysica status solidi (b) 1969, 36, 625–634 [https://onlinelibrary.wiley.com/doi/pdf/10.1002/pssb.19690360226]. doi:10.1002/pssb.19690360226.

[18] Kondo, S.i.; Nakamura, K. **Strain effects on the fundamental absorption in alkali iodides.** Journal of the Physical Society of Japan 1970, 28, 1381–1381, [https://doi.org/10.1143/JPSJ.28.1381].

doi:10.1143/JPSJ.28.1381.

[19] Erdinc, B.; Secuk, M.N.; Aycibin, M.; Gülebagan, S.E.; Dogan, E.K.; Akkus, H. **Ab-initio calculations of physical properties of alkali chloride XCl (X = K, Rb and Li) under pressure.** Computational Condensed Matter 2015, 4, 6–12. doi:https://doi.org/10.1016/j.cocom.2015.05.001.

[20] Shamp, A.; Saitta, P.; Zurek, E. **Theoretical predictions of novel potassium chloride phases under pressure.** Phys. Chem. Chem. Phys. 2015, 17, 12265–12272. doi:10.1039/C5CP00470E.

[21] Aguado, A. **Ga+ , In+ , and Tl+ impurities in alkali halide crystals: Distortion trends**. The Journal of Chemical Physics 2000, 113, 8680–8685, [https://doi.org/10.1063/1.1317520]. doi:10.1063/1.1317520.

[22] Bouhdjer, L.; Addala, S.; Chala, A.; Halimi, O.; Boudine, B.; Sebais, M. **Elaboration and characterization of a KCl single crystal doped with nanocrystals of a Sb_2O_3 semiconductor.** Journal of Semiconductors 2013, 34, 043001. doi:10.1088/1674-4926/34/4/043001.

[23] Myasnikova, A.; Mysovsky, A.; Paklin, A.; Shalaev, A. **Structure and optical properties of copper impurity in LiF and NaF crystals from ab initio calculations.** Chemical Physics Letters 2015, 633, 218–222. doi:https://doi.org/10.1016/j.cplett.2015.05.033.

[24] Daniel, D.J.; Ramasamy, P.; Madhusoodanan, U. **Optical properties and irradiation effects of Cu+ and Eu2+ doped alkali halide single crystals grown from melt using Czochralski technique.** Optik 2013, 124, 1466–1468. doi:https://doi.org/10.1016/j.ijleo.2012.03.089.

[25] Winter, N.W.; Pitzer, R.M.; Temple, D.K. **Theoretical study of a Cu+ ion impurity in a NaF host.** The Journal of Chemical Physics 1987, 86, 3549–3556, [https://doi.org/10.1063/1.451958]. doi:10.1063/1.451958.

[26] Preto, P.D.; Balraj, V.; Dhabekar, B.S.; Watanabe, S.; Rao, T.G.; Cano, N.F. **Synthesis, thermoluminescence, defect center and dosimetric characteristics of LiF:Mg,Cu,P,Si phosphor.** Applied Radiation and Isotopes 2017, 130, 21–28. doi:https://doi.org/10.1016/j.apradiso.2017.08.022.

[27] Preto, P.D.; Balraj, V.; Dhabekar, B.S.; Watanabe, S.; Rao, T.G. **Synthesis, thermoluminescence, defect centers and dosimetric characteristics of LiF:Mg,Cu,B phosphor.** Applied Radiation and Isotopes 2016, 118, 95–101. doi:https://doi.org/10.1016/j.apradiso.2016.08.015.

[28] Núñez-González, R.; Aceves, R.; Cabellos, J.L.; Posada-Amarillas, A. **Effect of substitutional Cu atoms on the electronic and optical properties of KCl: A DFT approach.** Materials Today Communications 2020, 22, 100831. doi:https://doi.org/10.1016/j.mtcomm.2019.100831.

[29] Goldberg, A.; McClure, D.; Pedrini, C. **Optical absorption and emission spectra of Cu+ : NaF single crystals.** Chemical Physics Letters 1982, 87, 508–511. doi:https://doi.org/10.1016/0009-2614(82)83023-6.

[30] Uhl, E.; Leitão, A.A.; Rocha, A.B. **Transition energies and oscillator strength calculated for d–s symmetry-forbidden electronic transition for Cu+ impurities in sodium fluoride host lattice.** Chemical Physics 2011, 389, 102–106. doi:https://doi.org/10.1016/j.chemphys.2011.08.011.

doi:10.20944/preprints202007.0433.v1

[31] Sun, Y.; Zhang, J.; Ding, J.; Yan, X. **First-principles study on electronic and optical properties of Cu-doped LiF with Li vacancy.** Physica B: Condensed Matter 2012, 407, 2458–2461. doi:https://doi.org/10.1016/j.physb.2012.03.046.

[32] Cabellos, J.L.; Mendoza, B.S.; Escobar, M.A.; Nastos, F.; Sipe, J.E. E**ffects of nonlocality on second-harmonic generation in bulk semiconductors.** Phys. Rev. B 2009, 80, 155205. doi:10.1103/PhysRevB.80.155205.

[33] Walker, D.; Verma, P.; Cranswick, L.; Jones, R.; Clark, S.; Buhre, S. **Halite-sylvite thermoelasticity**. American Mineralogist 2004, 89. doi:10.2138/am-2004-0124.

[34] Schwabegger, G.; Djuric, T.; Sitter, H.; Resel, R.; Simbrunner, C. **Morphological and structural investigation of sexithiophene growth on KCl (100).** Crystal Growth & Design 2013, 13, 536–542, [https://doi.org/10.1021/cg3010823]. PMID: 23413362, doi:10.1021/cg3010823.

[35] Li, J.; Duan, C.g.; Gu, Z.q.; Wang, D.s. **Linear optical properties and multiphoton absorption of alkali halides calculated from first principles.** Phys. Rev. B 1998, 57, 2222–2228. doi:10.1103/PhysRevB.57.2222.

[36] Aroyo, M.I.; Kirov, A.; Capillas, C.; Perez-Mato, J.M.; Wondratschek, H. Bilbao **Crystallographic Server. II. Representations of crystallographic point groups and space groups.** Acta Crystallographica Section A 2006, 62, 115–128. doi:10.1107/S0108767305040286.

[37] Setyawan, W.; Curtarolo, S. **High-throughput electronic band structure calculations: Challenges and tools.** Computational Materials Science 2010, 49, 299–312. doi:https://doi.org/10.1016/j.commatsci.2010.05.010.

[38] Cartoixa, X.; Palummo, M.; Hauge, H.I.T.; Bakkers, E.P.A.M.; Rurali, R. **Optical emission in hexagonal SiGe nanowires.** Nano Letters 2017, 17, 4753–4758, https://doi.org/10.1021/acs.nanolett.7b01441. PMID: 28654293, doi:10.1021/acs.nanolett.7b01441.

[39] Popescu, V.; Zunger, A. **Extracting E versus ~k effective band structure from supercell calculations on alloys and impurities.** Phys. Rev. B 2012, 85, 085201. doi:10.1103/PhysRevB.85.085201.

[40] Maspero, R.; Sweeney, S.J.; Florescu, M. **Unfolding the band structure of GaAsBi.** Journal of Physics: Condensed Matter 2016, 29, 075001. doi:10.1088/1361-648x/aa50d7.

[41] Dargam, T.G.; Capaz, R.B.; Koiller, B. **Disorder and size effects in the envelope-function approximation.** Phys. Rev. B 1997, 56, 9625–9629. doi:10.1103/PhysRevB.56.9625.

[42] Boykin, T.B.; Klimeck, G. **Practical application of zone-folding concepts in tight-binding calculations.** Phys. Rev. B 2005, 71, 115215. doi:10.1103/PhysRevB.71.115215.

[43] Popescu, V.; Zunger, A. **Effective band structure of random alloys.** Phys. Rev. Lett. 2010, 104, 236403. doi:10.1103/PhysRevLett.104.236403.

[44] Chen, M.; Weinert, M. **Layer k-projection and unfolding electronic bands at interfaces.** Phys. Rev. B 2018, 98, 245421. doi:10.1103/PhysRevB.98.245421.
[45] Lee, C.C.; Yamada-Takamura, Y.; Ozaki, T. **Unfolding method for first-principles LCAO electronic structure calculations.** Journal of Physics: Condensed Matter 2013, 25, 345501. doi:10.1088/0953-8984/25/34/345501.

[46] Ku, W.; Berlijn, T.; Lee, C.C. **Unfolding first-principles band structures.** Phys. Rev. Lett. 2010, 104, 216401. doi:10.1103/PhysRevLett.104.216401.

[47] Allen, P.B.; Berlijn, T.; Casavant, D.A.; Soler, J.M. **Recovering hidden Bloch character: Unfolding electrons, phonons, and slabs.** Phys. Rev. B 2013, 87, 085322. doi:10.1103/PhysRevB.87.085322.

[48] Rubel, O.; Bokhanchuk, A.; Ahmed, S.J.; Assmann, E. **Unfolding the band structure of disordered solids: From bound states to high-mobility Kane fermions.** Phys. Rev. B 2014, 90, 115202. doi:10.1103/PhysRevB.90.115202.

[49] Medeiros, P.V.C.; Stafström, S.; Björk, J. **Effects of extrinsic and intrinsic perturbations on the electronic structure of graphene: Retaining an effective primitive cell band structure by band unfolding.** Phys. Rev. B 2014, 89, 041407. doi:10.1103/PhysRevB.89.041407.

[50] Medeiros, P.V.C.; Tsirkin, S.S.; Stafström, S.; Björk, J. **Unfolding spinor wave functions and expectation values of general operators: Introducing the unfolding-density operator.** Phys. Rev. B 2015, 91, 041116. doi:10.1103/PhysRevB.91.041116.

[51] Huang, H.; Zheng, F.; Zhang, P.; Wu, J.; Gu, B.L.; Duan, W. **A general group theoretical method to unfold band structures and its application.** New Journal of Physics 2014, 16, 033034. doi:10.1088/1367-2630/16/3/033034.

[52] Kosugi, T.; Nishi, H.; Kato, Y.; Matsushita, Y.i. **Periodicity-free unfolding method of electronic energy spectra.** Journal of the Physical Society of Japan 2017, 86, 124717, [https://doi.org/10.7566/JPSJ.86.124717]. doi:10.7566/JPSJ.86.124717.

[53] Mayo, S.G.; Yndurain, F.; Soler, J.M. **Band unfolding made simple.** Journal of Physics: Condensed Matter 2020, 32, 205902. doi:10.1088/1361-648x/ab6e8e.

[54] Dombrowski, D.; Jolie, W.; Petrović, M.; Runte, S.; Craes, F.; Klinkhammer, J.; Kralj, M.; Lazić, P.; Sela, E.; Busse, C. **Energy-dependent chirality effects in quasifree-standing graphene.** Phys. Rev. Lett. 2017, 118, 116401. doi:10.1103/PhysRevLett.118.116401.

[55] Warmuth, J.; Bruix, A.; Michiardi, M.; Hänke, T.; Bianchi, M.; Wiebe, J.; Wiesendanger, R.; Hammer, B. Hofmann, P.; Khajetoorians, A.A. **Band-gap engineering by Bi intercalation of graphene on Ir(111).** Phys Rev. B 2016, 93, 165437. doi:10.1103/PhysRevB.93.165437.

[56] Abdollahi, A.; Golzan, M.M.; Aghayar, K. **Electronic properties of GaxIn1-xP ternary alloy from first-principles.** Computational Materials Science 2016, 120, 70–76. doi:https://doi.org/10.1016/j.commatsci.2016.04.010.

[57] Molina-Sánchez, A.; Sangalli, D.; Hummer, K.; Marini, A.; Wirtz, L. **Effect of spin-orbit**

interaction on the optical spectra of single-layer, double-layer, and bulk MoS2. Phys. Rev. B 2013, 88, 045412. doi:10.1103/PhysRevB.88.045412.
[58] Sipe, J.E.; Shkrebtii, A.I. **Second-order optical response in semiconductors.** Phys. Rev. B 2000, 61, 5337–5352 doi:10.1103/PhysRevB.61.5337.

[59] Salazar, C.; Cheng, J.L.; Sipe, J.E. **Coherent control of current injection in zigzag graphene nanoribbons.** Phys. Rev. B 2016, 93, 075442. doi:10.1103/PhysRevB.93.075442.

[60] Lee, M.H.; Yang, C.H.; Jan, J.H. **Band-resolved analysis of nonlinear optical properties of crystalline and molecular materials.** Phys. Rev. B 2004, 70, 235110. doi:10.1103/PhysRevB.70.235110.

[61] Nastos, F.; Olejnik, B.; Schwarz, K.; Sipe, J.E. **Scissors implementation within length-gauge formulations of the frequency-dependent nonlinear optical response of semiconductors.** Phys. Rev. B 2005, 72, 045223. doi:10.1103/PhysRevB.72.045223.

[62] Stahrenberg, K.; Herrmann, T.; Wilmers, K.; Esser, N.; Richter, W.; Lee, M.J.G. **Optical properties of copper and silver in the energy range 2.5–9.0 eV.** Phys. Rev. B 2001, 64, 115111. doi:10.1103/PhysRevB.64.115111.

[63] Reshak, A.H.; Chen, X.; Auluck, S.; Kamarudin, H. **Linear and nonlinear optical susceptibilities and hyperpolarizability of borate LiNaB4O7 single crystals: Theory and experiment.** Journal of Applied Physics 2012, 112, 053526, [https://doi.org/10.1063/1.4749409]. Doi:10.1063/1.4749409.

[64] Okoye, C.M.I. **Theoretical study of the electronic structure, chemical bonding and optical properties of KNbO3in the paraelectric cubic phase.** Journal of Physics: Condensed Matter 2003, 15, 5945–5958. doi:10.1088/0953-8984/15/35/304.

[65] Leitsmann, R.; Schmidt, W.G.; Hahn, P.H.; Bechstedt, F. **Second-harmonic polarizability including electron-hole attraction from band-structure theory.** Phys. Rev. B 2005, 71, 195209. doi:10.1103/PhysRevB.71.195209.

[66] Gonze, X.; Jollet, F.; Araujo, F.A.; Adams, D.; Amadon, B.; Applencourt, T.; Audouze, C.; Beuken, J.M.; Bieder, J.; Bokhanchuk, A.; Bousquet, E.; Bruneval, F.; Caliste, D.; Côté, M.; Dahm, F.; Pieve, F.D.; Delaveau, M.; Gennaro, M.D.; Dorado, B.; Espejo, C.; Geneste, G.; Genovese, L.; Gerossier, A.; Giantomassi, M.; Gillet, Y.; Hamann, D.; He, L.; Jomard, G.; Janssen, J.L.; Roux, S.L.; Levitt, A.; Lherbier, A.; Liu, F.; Lukačević, I.; Martin, A.; Martins, C.; Oliveira, M.; Poncé, S.; Pouillon, Y.; Rangel, T.; Rignanese, G.M.; Romero, A.; Rousseau, B.; Rubel, O.; Shukri, A.; Stankovski, M.; Torrent, M.; Setten, M.V.; Troeye, B.V.; Verstraete, M.; Waroquiers, D.; Wiktor, J.; Xu, B.; Zhou, A.; Zwanziger, J. **Recent developments in the ABINIT software package.** Computer Physics Communications 2016, 205, 106–131. doi:https://doi.org/10.1016/j.cpc.2016.04.003.

[67] Gonze, X.; Amadon, B.; Anglade, P.M.; Beuken, J.M.; Bottin, F.; Boulanger, P.; Bruneval, F.; Caliste, D.; Caracas, R.; Côté, M.; Deutsch, T.; Genovese, L.; Ghosez, P.; Giantomassi, M.; Goedecker, S.; Hamann, D.; Hermet, P.; Jollet, F.; Jomard, G.; Leroux, S.; Mancini, M.; Mazevet, S.; Oliveira, M.; Onida, G.; Pouillon, Y.; Rangel, T.; Rignanese, G.M.; Sangalli, D.; Shaltaf, R.; Torrent, M.; Verstraete, M.; Zerah, G.; Zwanziger, J. **ABINIT: First-principles approach to material and nanosystem properties**. Computer Physics Communications 2009, 180, 2582–2615. 40 YEARS OF CPC: A celebratory issue focused on quality software for high performance, grid and novel computing

architectures, doi:https://doi.org/10.1016/j.cpc.2009.07.007.

[68] Hamann, D.R. **Optimized norm-conserving Vanderbilt pseudopotentials.** Phys. Rev. B 2013, 88, 085117. doi:10.1103/PhysRevB.88.085117.

[69] Perdew, J.P.; Burke, K.; Ernzerhof, M. **Generalized gradient approximation made simple.** Phys. Rev. Lett 1996, 77, 3865–3868. doi:10.1103/physrevlett.77.3865.

[70] Monkhorst, H.J.; Pack, J.D. **Special points for Brillouin-zone integrations.** Phys. Rev. B 1976, 13, 5188–5192 doi:10.1103/PhysRevB.13.5188.

[71] Persson, K. **Materials data on KCl (SG:225)** by Materials Project, 2014. An optional note, doi:10.17188/1199313.

[72] Roessler, D.M.; Walker, W.C. Electronic Spectra of Crystalline NaCl and KCl. Phys. Rev. 1968, 166, 599–606. doi:10.1103/PhysRev.166.599.

[73] Phillips, J.C. Ultraviolet Absorption of Insulators. III. fcc Alkali Halides. Phys. Rev. 1964, 136, A1705–A1713. doi:10.1103/PhysRev.136.A1705.

[74] Jones, R.O.; Gunnarsson, O. **The density functional formalism, its applications and prospects**. Rev. Mod. Phys. 1989, 61, 689–746. doi:10.1103/RevModPhys.61.689.

[75] Boykin, T.B.; Klimeck, G. **Practical application of zone-folding concepts in tight-binding calculations.** Phys. Rev. B 2005, 71, 115215. doi:10.1103/PhysRevB.71.115215.

[76] Boykin, T.B.; Kharche, N.; Klimeck, G.; Korkusinski, M. **Approximate bandstructures of semiconductors alloys from tight-binding supercell calculations.** Journal of Physics: Condensed Matter 2007, 19, 036203. doi:10.1088/0953-8984/19/3/036203.

[77] Deretzis, I.; Calogero, G.; Angilella, G.G.N.; Magna, A.L., **Role of basis set on the unfolding of supercell band structure: From tight-binding to density functional thoery** EPL (Europhysics Letters) 2014, 107, 27006. doi:10.1209/0295-5075/107/27006.

[78] Dai, Z.H.; Xie, Y.P.; Qian, Y.C.; Hu, L.J.; Li, X.D.; Ma, H.T., **Effects of P, As, and Sb heavy doping on band gap narrowing of germanium as light emmitting materials** 2017, [arXiv:cond-mat.mtrl-sci/1706.04050].

[79] Onida, G.; Reining, L.; Rubio, A.**, Electronic excitations: Density-functional versus many-body Greeen's function approaches** Rev. Mod. Phys. 2002, 74, 601–659. doi:10.1103/RevModPhys.74.601.

[80] Hybertsen, M.S.; Louie, S.G.**, Electron correlation in semiconductors and insulators: band gaps and quasiparticule energies.** Phys. Rev. B 1986, 34, 5390–5413. doi:10.1103/PhysRevB.34.5390.

[81] Fox, M. **Optical Properties of Solids**; p. 288., Oxford master series in condensed matter physics, Oxford University Press, 2001, New York.